Editors' Suggestion

Influence of boundary conditions on rapidly rotating convection and its dynamo action in a plane fluid layer

Patrick Kolhey[1,*] Stephan Stellmach,[2] and Daniel Heyner[1]
[1]*Institut für Geophysik und extraterrestrische Physik, Technische Universität Braunschweig, D-38106 Braunschweig, Germany*
[2]*Institut für Geophysik, Westfälische Wilhelms-Universität, D-48149 Münster, Germany*

(Received 9 December 2021; accepted 25 February 2022; published 5 April 2022)

The Childress-Soward model, consisting of a an electrically conducting Rayleigh-Bénard layer rotating about a vertical axis, is the conceptually simplest model configuration that captures all essentials of convectively driven dynamos. Here we study the effects of different boundary conditions on this type of dynamo. This closes a gap in the existing literature, which has primarily focused on simple, but geophysically not very realistic, cases. Furthermore, the extensive literature on boundary layers in nonrotating and rotating Rayleigh-Bénard convection makes the Childress-Soward model an ideal test bed for illuminating the fundamental effects that the boundary conditions have on convection-driven dynamos. In this study we systematically vary the thermal, mechanical, and electrical boundary conditions in direct numerical simulations, with a focus on flow regimes characterized by geostrophic turbulence. One key result applies to both dynamos and nonmagnetic, rotating convection. We show that for no-slip boundaries, the Nusselt number increases significantly when a fixed heat flux is imposed instead of a given temperature difference. This effect can be explained by an interplay of Ekman pumping and the internal structure of the thermal boundary layer, which is very sensitive to thermal boundary conditions. Dynamical changes are shown to exist only within the boundary layers, such that the bulk dynamics remains largely unaffected. In the dynamo case, we argue that care needs to be taken in order to ensure comparable energetics when changing from fixed-temperature to fixed-flux conditions. If done properly, no significant differences in the leading order features of the resulting dynamos are observed. In particular, the thermal boundary conditions have no noticeable influence on the horizontal flow scales, as might have been expected from studies in spherical geometry. In contrast, the mechanical boundary conditions largely control whether or not large-scale flows and fields can be generated. For no-slip boundaries, Ekman friction strongly suppresses upscale transport and eliminates the large-scale vortex dynamos that exist in the stress-free case. Finally, the magnetic boundary conditions are shown to strongly affect the topology of the generated magnetic fields. For an insulating exterior, the magnetic field is most intense in the central part of the fluid layer, whereas we observe a strong magnetic field buildup close to perfectly conducting boundaries. For large magnetic Reynolds numbers, we further observe thin layers of intense horizontal field attached to perfect conductors. The horizontal flow scales, however, remain largely unaffected in the investigated parameter regime.

DOI: 10.1103/PhysRevFluids.7.043502

*p.kolhey@tu-braunschweig.de

I. INTRODUCTION

The large-scale magnetic fields of most geo- and astrophysical objects, including the Earth's magnetic field, are generated by fluid motions in their electrically conducting interiors. In most cases, these motions are thought to be driven by buoyancy forces, with Coriolis forces organizing the flow in a way that promotes magnetic field generation. The conceptually simplest model configuration combining the effects of convection, rotation, and electromagnetic induction is the so-called Childress-Soward model [1], which is the focus of this paper. It consists of a plane layer of electrically conducting fluid that is heated from below, cooled from above, and rotates about a vertical axis.

Without rotation and electromagnetic induction, the Childress-Soward configuration is nothing but the classical Rayleigh-Bénard system, which is the most comprehensively studied convective system to date. Laboratory experiments as well as theoretical work on convective flows usually employ this setting. In fact, almost everything we know about the fundamental properties of convection has been established in the context of the Rayleigh-Bénard configuration [2], which has also been of crucial importance in developing our current understanding of nonmagnetic, rotating convection. This large body of existing knowledge, which has grown significantly since Childress and Soward proposed their model in the early 1970s, makes the configuration particularly attractive.

A central corner stone in almost all theories of nonrotating Rayleigh-Bénard convection are boundary layers, whose existence and properties depend on the boundary conditions applied. Boundary layers are known to control the transport properties, regime transitions, and certain properties of the bulk flow over a large fraction of parameter space [3–10]. The question when and even if boundary layers ever lose their controlling influence in highly turbulent convection, resulting in a so-called "ultimate" regime [11,12], is a matter of ongoing research [13,14]. As the characteristics of boundary layers are determined by the physical nature of the bounding surfaces, the role of boundary conditions in Rayleigh-Bénard convection has also been studied thoroughly [8,15,16].

The extent to which boundary conditions matter in rotating Rayleigh-Bénard convection has also received considerable attention. Similar to the nonrotating case, both transport properties as well as regime transitions have been tied to boundary layer dynamics [17–23]. The fact that rotation turns the viscous boundary layer into an Ekman layer has important consequences not just for the transport properties [20,21,23,24], but also for the leading order flow within the bulk. Different from the nonrotating case, the formation of an intense, coherent, large-scale circulation in the turbulent regime (taking the form of a large-scale barotropic vortex in the rotating case) can be hampered by rigid, no-slip boundaries [20,22,24,25].

The importance of boundary layers in the rotating and nonrotating Rayleigh-Bénard system suggests that the dynamics of the Childress-Soward dynamo model may also depend to some degree on the nature of the physical boundaries. In this case, the magnetic diffusivity enters the problem as a third diffusion coefficient, such that a magnetic boundary condition has to be specified in addition to the thermal and mechanical ones. Somewhat surprisingly, however, no systematic attempt has been made to study the influence of different boundary conditions for the Childress-Soward model. A possible reason may be that the popularity of the model mainly stems from its conceptual simplicity, which can be maximized by choosing simple boundary conditions. The choice of free-slip boundaries largely suppresses viscous boundary layers, substantially lowering the cost of numerical simulations while eliminating the rich dynamics caused by dynamically active Ekman layers [21]. The magnetic boundary conditions become very simple (and mathematically analogous to a free-slip mechanical boundary condition) if the exterior is assumed to be a perfect electrical conductor, removing the need to consider the field behavior in the external region. Finally, for simplicity the boundaries are usually assumed to be perfect thermal conductors, such that they are able to sustain a given temperature value. While this eliminates lateral temperature gradients on the boundary, it differs from many geo- and astrophysical systems, where external processes often control the heat flux through the convective layer. In summary, the choice of stress-free, fixed-temperature, and

electrically perfectly conducting boundary conditions simplifies the physical problem considerably and greatly reduces the costs of direct numerical simulations. Following Roberts and Jones [26], we will call this particular choice *illustrative boundary conditions* in the following. Apart from few exceptions [27,28], the large majority of previous studies have employed these simple, illustrative boundary conditions [29–37].

It may be argued that if one is willing to sacrifice spherical geometry in an attempt to maximize simplicity, the choice of simple boundary conditions may as well be justified. However, this view ignores the extensive work on the (rotating) Rayleigh-Bénard system that suggest that boundary conditions and the related boundary layers can be of prime importance for the dynamics. It also eliminates the opportunity to exploit the simplicity of the Childress-Soward configuration for studying the effects of boundary conditions on convectively driven dynamos in a simple and illustrative setting. The goal of this paper is to make a step in this direction.

While no systematic study on the effect of different boundary conditions on Cartesian dynamos exists, the literature nevertheless contains a number of clues, observations and speculations on the subject, which are reviewed below. In order to keep the text within reasonable bounds, we largely focus on the Cartesian case here, although we will briefly mention results obtained using spherical shell models where appropriate.

For the thermal boundary condition, imposing either a fixed temperature and or a fixed heat flux at the boundaries are important end-member cases. In pure Rayleigh-Bénard convection, it is well known that an imposed heat flux enforces wide aspect ratio cells at onset [38], which continue to dominate at moderate Rayleigh number [39]. In the high Rayleigh number regime, the heat transport characteristics appear to be largely identical for both choices of thermal boundary conditions [15,40]. Interestingly, the thermal boundary conditions still seem to remain important for the flow field, where they have been shown to control the statistical properties of the large-scale circulation, in particular its amplitude and reversal frequency [9]. Furthermore, they promote supergranule aggregation in wide aspect ratio cells [41]. When Coriolis forces are added to the system, instructive results have been obtained for the asymptotic case of rapid rotation. Here theory suggests that both types of thermal boundary conditions lead to the same dynamical behavior. In the linear case, this was demonstrated by Takehiro *et al.* [42]. Calkins *et al.* [43] have confirmed this result. They have further demonstrated the equivalence of fixed-heat-flux and fixed-temperature boundary conditions in the framework of nonhydrostatic, quasigeostrophic theory for the special case of stress-free mechanical boundaries. An important first result of our paper is that for the bulk flow these results continue to hold for finite rotation rates and rigid boundaries with remarkable accuracy. In particular, we will demonstrate that the bulk flow in all major regimes that have been identified in rotationally constrained convection [20,44,45] is essentially insensitive to the choice either fixed-flux or fixed-temperature boundary conditions. However, the Ekman pumping occurring in the vicinity of the rigid boundaries increases the Nusselt number significantly (by up to $\sim$10%) as compared to the fixed-temperature case. To our knowledge, this effect of the thermal boundary condition has not been reported in the existing literature of nonmagnetic, rotating convection.

If both rotation and magnetic fields are present, it has been argued that the type of thermal boundary condition may also affect the bulk flow significantly. Studies employing a spherical shell geometry have established that the specific choice of the thermal boundary condition can drastically change the solution structure in the magnetic case [46–48]. In particular, dynamo simulations have been presented in which a constant heat flux strongly helps the magnetic field in generating planetary-scale flow structures. With fixed-temperature boundary conditions but an otherwise identical simulation setup, this effect is largely absent. Instead, the flow retains the typical rotation-induced small-scale structure and is little affected by the magnetic field. Hori *et al.* [47] rationalized this observation using linear magneto-convection results in a plane layer, where a purely vertical magnetic field is imposed. They show that in this setting, the heat flux boundary condition allows for wider convection cells at onset, characterized by a much larger range of unstable long-wavelength modes than found for fixed-temperature boundary conditions. However, it remains questionable how far these linear results carry over into the nonlinear dynamo

regime. Furthermore, a dynamo generated magnetic field differs strongly from the uniform magnetic field assumed in the linear magneto-convection case. The role of the thermal boundary condition for Childress-Soward-type dynamos is thus unclear. We will demonstrate below that, at least in the geophysically most relevant regime of geostrophic turbulence, the flow scales remain largely insensitive to the thermal boundary condition, despite the arguments presented in [47].

Different from the thermal boundary condition, the choice of the mechanical boundary condition is known to strongly affect the flow structure in the nonmagnetic case. As already pointed out above, the presence of Ekman layers and the resulting enhancement of heat transport due to Ekman pumping is generally not negligible when boundaries are assumed to be rigid [20,21,24]. Furthermore, Ekman friction is known to attenuate the efficiency of up-scale energy transport, preventing the formation of a coherent vortex condensate [20,22,24] and giving rise to intermittent behavior instead. The consequences for Cartesian dynamos have not been studied so far to our best knowledge. We will show below that Ekman layers in fact largely suppress the generation of large-scale flows and magnetic fields in the parameter regime studied, in contrast to the free-slip, illustrative case [34,49].

Finally, little is known concerning the effect of the magnetic boundary conditions. Here an electrically insulating or a perfectly conducting exterior region are the relevant end-member cases. St. Pierre [29] assumed electrically perfectly conducting boundaries in his simulations and reported a strong buildup of magnetic energy close to the boundaries, which could lead to increased effects of Lorentz forces in these regions. Furthermore, Jones and Roberts [27] have pointed out that different magnetic boundary conditions pose different constraints on the topology on the mean magnetic fields that can be generated by the dynamo. In order to avoid the nonlocal coupling introduced by an insulating exterior region, several authors have applied so-called *pseudovacuum* boundary conditions instead, which crudely approximate the insulating case by enforcing a purely vertical field at the boundary. Some of them compared solutions obtained for perfectly conducting boundaries to solutions obtained for the pseudovacuum case. For example, Thelen and Cattaneo [50] carried out a study of nonrotating dynamos and reported that the dynamo mechanism in the bulk region remains almost unaffected, while the field morphology and amplitude close to the boundaries shows more significant changes. Guervilly *et al.* [49] briefly mention that the main characteristics of their turbulent dynamo simulations remain largely unchanged when switching from perfectly conducting to pseudovacuum conditions. In contrast, Bushby *et al.* [51] found more extreme differences in their compressible dynamo simulations, where pseudovacuum boundary conditions allowed for the generation of a large-scale magnetic field, while only a small-scale field was observed in the perfectly conducting case. We will demonstrate below that the magnetic field topology indeed depends strongly on the magnetic boundary conditions. Furthermore, we show that thin layers of intense horizontal field tend to form adjacent to perfect conductors. We argue that these represent a challenge for Fourier-based simulations codes which are usually employed to study the illustrative case as these methods lack the opportunity to refine the grid towards the boundaries.

In summary, the main goal of this paper is to shed light on the dynamical role of the boundary conditions in plane layer dynamos. Because of the four-dimensional control parameter space and because many different combinations of mechanical, thermal, and magnetic boundary conditions exist, it is impossible for a single study to cover all possible cases. We therefore strive for a compromise that ensures that all cases lie within the geophysically most interesting geostrophic turbulence regime, as previously investigated by Guervilly *et al.* [34]. Furthermore, in terms of boundary conditions, we will focus only on the relevant end-member cases, i.e., stress-free or no-slip conditions for velocity, fixed-temperature, or fixed-flux conditions for the thermal field and electrically insulating or perfectly conducting exterior regions for the magnetic field. We note in passing that in real geophysical and astrophysical bodies, more complicated conditions usually apply.

The paper is organized as follows. In the next section, we describe the model in mathematical terms and define some useful quantities. The results are presented in Sec. III, where we begin by exploring the effect of the thermal boundary conditions on rotating, nonmagnetic convection in

Sec. III A. Dynamo simulations are discussed in Sec. III B. The paper concludes with a discussion in Sec. IV.

II. MODEL DESCRIPTION

A. Governing equations and boundary conditions

In this study we consider a rotating Cartesian plane layer model, consisting of an electrically conducting Boussinesq fluid confined between parallel, impenetrable walls at $z \in \{0, d\}$. We assume horizontal periodicity in the x and y directions over a length scale ℓ. The system rotates about the vertical axis with constant angular velocity $\boldsymbol{\Omega} = \Omega\, \boldsymbol{e}_z$, where $\boldsymbol{e}_z$ denotes the unit vector in the z direction, with gravity pointing downward, $\boldsymbol{g} = -g\, \boldsymbol{e}_z$. The fluid is heated from below and cooled from above, with either a constant temperature drop ΔT being imposed across the layer or a constant temperature gradient β being maintained at the boundaries (constant heat flux). The fluid has constant density ρ, kinematic viscosity ν, thermal diffusivity κ, thermal expansion coefficient α and magnetic diffusivity η. Nondimensional equations for the conservation of mass, momentum transport, temperature transport, and induction are obtained by scaling length with the layer depth d, time with the thermal diffusion time d^2/κ, temperature with either the temperature difference ΔT, or the temperature gradient βd, depending on the thermal boundary conditions, and magnetic field strength with $(\nu\rho\eta\mu_0)^{1/2}/d$ (where μ_0 is the permeability in free space). The governing equations then take the form

$$\boldsymbol{\nabla} \cdot \boldsymbol{u} = 0, \tag{1}$$

$$\boldsymbol{\nabla} \cdot \boldsymbol{B} = 0, \tag{2}$$

$$\frac{\partial \boldsymbol{u}}{\partial t} + (\boldsymbol{u} \cdot \boldsymbol{\nabla})\boldsymbol{u} = -\boldsymbol{\nabla} p + \mathrm{Ra}\,\mathrm{Pr}\, T\, \boldsymbol{e}_z - \frac{\mathrm{Pr}}{E}\boldsymbol{e}_z \times \boldsymbol{u} + \frac{\mathrm{Pr}}{q}(\boldsymbol{\nabla} \times \boldsymbol{B}) \times \boldsymbol{B} + \mathrm{Pr}\,\nabla^2 \boldsymbol{u}, \tag{3}$$

$$\frac{\partial T}{\partial t} + (\boldsymbol{u} \cdot \boldsymbol{\nabla})T = \nabla^2 T, \tag{4}$$

$$\frac{\partial \boldsymbol{B}}{\partial t} = \boldsymbol{\nabla} \times (\boldsymbol{u} \times \boldsymbol{B}) + \frac{1}{q}\nabla^2 \boldsymbol{B}. \tag{5}$$

Here $\boldsymbol{u} = (u, v, w)$ denotes the velocity field, $\boldsymbol{B} = (B_x, B_y, B_z)$ the magnetic field, p the modified pressure (which contains the centrifugal pressure), and T the temperature, using the above scaling. The resulting control parameters are the Ekman number E, the Rayleigh number Ra, the Prandtl number Pr, the Roberts number q, and the aspect ratio Γ, which are defined by

$$E = \frac{\nu}{2\Omega d^2}, \quad \mathrm{Ra_{FT}} = \frac{\alpha g \Delta T d^3}{\nu\kappa}, \quad \text{or} \quad \mathrm{Ra_{FF}} = \frac{\alpha g \beta d^4}{\nu\kappa}, \quad \mathrm{Pr} = \frac{\nu}{\kappa}, \quad q = \frac{\kappa}{\eta}, \quad \Gamma = \ell/d.$$

Note that two different forms of the Rayleigh number appear, depending on the thermal boundary condition used. These are distinguished by subscripts, which indicate whether a fixed-temperature (FT) boundary condition or a fixed-heat-flux (FF) boundary condition is applied.

Our study investigates the effects of employing different sets of boundary conditions. While the boundary conditions in natural objects are often complicated, we focus on the most important end member cased here. The mechanical boundary conditions are either stress-free

$$\frac{\partial u}{\partial z} = \frac{\partial v}{\partial z} = w = 0 \quad \text{at} \quad z \in \{0, 1\}, \tag{6}$$

or no-slip

$$u = v = w = 0 \quad \text{at} \quad z \in \{0, 1\}. \tag{7}$$

For the temperature, the boundaries are either held at fixed temperature,

$$T(z = 0) = 1 \quad \text{and} \quad T(z = 1) = 0, \tag{8}$$

or a fixed temperature gradient

$$\frac{\partial T}{\partial z} = -1 \quad \text{at} \quad z \in \{0, 1\} \tag{9}$$

is imposed. Two popular choices exist for the magnetic boundary conditions. First, there is the possibility of an electrically perfectly conducting exterior region, such that

$$\frac{\partial B_x}{\partial z} = \frac{\partial B_y}{\partial z} = B_z = 0 \quad \text{at} \quad z \in \{0, 1\} \tag{10}$$

applies at the boundaries. The second choice is an electrically insulating exterior region, resulting in a harmonic magnetic field ($\nabla^2 \boldsymbol{B} = 0$) outside the layer which tends to zero as $|z| \to \infty$. More details on the formulation of the magnetic boundary conditions in terms of poloidal and toroidal potentials, as used in our simulation code, are given by Roberts and Jones [26] and Jones and Roberts [27]. Both electrically insulating and perfectly conducting boundaries are considered in this study.

B. Numerical method

The governing equations (1)–(5) are solved numerically using a modified version of the pseudospectral code developed by Stellmach and Hansen [52]. In particular, for this study, the possibility to solve the system with a fixed heat flux at the boundaries has been added to the code.

C. Diagnostics

In order to compare different sets of simulations we use the following diagnostic output parameters. The heat flux across the system is quantified by the Nusselt number, which we define as

$$\mathrm{Nu} = \frac{\langle (\boldsymbol{u}T - \boldsymbol{\nabla} T) \cdot \boldsymbol{e}_z \rangle_{\mathrm{Vol}}}{\langle -\boldsymbol{\nabla} T \cdot \boldsymbol{e}_z \rangle_{\mathrm{Vol}}}, \tag{11}$$

where $\langle \dots \rangle_{\mathrm{Vol}}$ denotes the volume average over the fluid layer. Due to the different thermal boundary conditions one obtains for the fixed-temperature boundary condition

$$\mathrm{Nu}_{FT} = \langle wT - \partial_z T \rangle_{\mathrm{Vol}}, \tag{12}$$

whereas with a fixed heat flux the Nusselt number is defined as

$$\mathrm{Nu}_{FF} = 1 + \frac{\langle wT \rangle_{\mathrm{Vol}}}{\Delta T}. \tag{13}$$

Note that in the last formula, $\Delta T = \langle T(z=0) \rangle_{xy} - \langle T(z=1) \rangle_{xy}$ denotes the mean temperature difference between the top and bottom boundary, where $\langle \dots \rangle_{xy}$ is the horizontal average.

A further diagnostic parameter, quantifying the vigor of the convective flow, is the Reynolds number

$$\mathrm{Re} = \frac{\sqrt{\langle \mathbf{u}^2 \rangle_{\mathrm{Vol}}}}{\mathrm{Pr}}, \tag{14}$$

defined as the ratio of the viscous to the advective timescale.

In addition to these global diagnostics, we also calculate one-dimensional energy spectra in order to investigate the distribution of kinetic and magnetic energy across different scales. We divide the horizontal kinetic energy into barotropic and baroclinic components

$$E_{\mathrm{kin},bt} = \frac{1}{2}(\langle u^2 \rangle_z + \langle v^2 \rangle_z), \tag{15}$$

$$E_{\mathrm{kin},bc} = \frac{1}{2}(u'^2 + v'^2), \tag{16}$$

where $\langle \dots \rangle_z$ denotes a vertical average and $u_i'(x, y, z) = u_i(x, y, z) - \langle u_i(x, y) \rangle_z$. The energy spectrum for the barotropic kinetic energy is calculated by

$$E_{\mathrm{kin},bt}(k_h) = \frac{1}{2} \sum_{k_x, k_y \in r_{k_h}} (|\widehat{\langle u \rangle}_z(k_x, k_y)|^2 + |\widehat{\langle v \rangle}_z(k_x, k_y)|^2), \tag{17}$$

where $k_h = \sqrt{k_x^2 + k_y^2}$ is the horizontal wave number and $\widehat{\langle u_i \rangle}_z$ is the Fourier transformed vertically averaged velocity component. The spectrum is calculated by binning the energy into rings r_{k_h} of radius $k_h - 0.5\Delta_k \leqslant \sqrt{k_x^2 + k_y^2} \leqslant k_h + 0.5\Delta_k$ where $\Delta_k = 2\pi/\Gamma$ is the step size and $k_h = 2\pi k/\Gamma$ with $k = 0, 1, 2, \dots$. Energy spectra for the baroclinic kinetic energy component, the horizontal magnetic field $\boldsymbol{B}_h = (B_x, B_y, 0)$, and the vertical magnetic field B_z are calculated equivalently. Note that additional vertical averaging over the fluid layer is performed for these spectral energies, since otherwise the spectra would still be dependent on the vertical coordinate z.

D. Comparing simulations with different thermal boundary conditions

Different definitions are used for the Rayleigh number for fixed-flux and fixed-temperature boundary conditions. In order to allow for a meaningful comparison, we usually begin by running a simulation with fixed-temperature boundary conditions and measure the time-averaged heat flux across the layer. This heat flux is then imposed in a corresponding simulation using fixed-flux boundary conditions. This procedure requires us to choose the Rayleigh number in the fixed-flux case according to

$$\mathrm{Ra}_{FF} = \mathrm{Nu}_{FT}\, \mathrm{Ra}_{FT}. \tag{18}$$

Alternatively, we could have also begun by running simulations for the fixed-flux case. From the average temperature jump ΔT that is established across the layer, a Rayleigh number for the fixed-temperature case can then be constructed as $\mathrm{Ra}_{FT} = \mathrm{Ra}_{FF}/\mathrm{Nu}_{FF}$. The reason for choosing Eq. (18) is that this procedure guarantees that the same amount of power is supplied to the system in both cases.

In order to compare results obtained for different thermal boundary conditions in a quantitative fashion, the dimensionless temperature field also needs proper rescaling. Here we use

$$T_{FT} = \mathrm{Nu}_{FT}\, (T_{FF} - \langle T_{FF} \rangle_{\mathrm{Vol}}) + 0.5 \tag{19}$$

to convert the dimensionless temperature values T_{FF} obtained in fixed-flux simulations to "equivalent" fixed-temperature values T_{FT}. Note that the mean temperature $\langle T_{FF} \rangle_{\mathrm{Vol}}$ needs to be subtracted before multiplying by Nu_{FT} because it is purely determined by the randomly chosen initial temperature distribution for fixed-flux boundary conditions.

III. RESULTS

A. Nonmagnetic convection

The role of the mechanical boundary conditions in rotating convection has been investigated thoroughly in a number of recent publications [20–24]. For this reason, we will not explore it further here. Instead, we will focus on the role of the thermal boundary conditions which have received much less attention so far.

A few results concerning the role of the thermal boundary conditions in rapidly rotating convection have been published previously in literature. The linear stability properties have been examined for both fixed-temperature and fixed-flux boundary conditions. In particular, for stress-free mechanical boundary conditions, it has been shown that in the limit $E \to 0$, the onset of convection occurs at the same critical Rayleigh and wave numbers in both cases [42,43]. In the low Ekman number regime, the parameters

$$\widetilde{\mathrm{Ra}}_{FT} = E^{4/3}\mathrm{Ra}_{FT} \quad \text{and} \quad \widetilde{\mathrm{Ra}}_{FF} = E^{4/3}\mathrm{Ra}_{FF} \tag{20}$$

can then be used as a proxy for supercriticality. An asymptotically reduced model for the rotationally constrained regime has been developed by Calkins *et al.* [43], also with a focus on the stress-free case. They argue that in the rapidly rotating regime, the leading order dynamics is equivalent for both types of thermal boundary conditions if the Rayleigh numbers are chosen according to Eq. (18), or, put into a form more suitable for the asymptotic case, if $\widetilde{\mathrm{Ra}}_{FF} = \mathrm{Nu}_{FT}\,\widetilde{\mathrm{Ra}}_{FT}$.

The first goal of our study is to investigate whether this result already holds for the moderate Ekman numbers achievable in direct numerical simulations. If it does, another important question is whether it also applies to no-slip boundaries. In order to answer these questions, we compare results from a suite of numerical simulations at $E = 10^{-5}$ employing different sets of boundary conditions. Results from a previous paper [20] were used for the fixed-temperature case. From this data, the associated flux Rayleigh numbers were calculated by Eq. (18), and simulations for the fixed-flux case were performed for both stress-free and no-slip boundary conditions. In Table I important input and output quantities are summarized.

The typical spatial structures observed in our simulations are summarized in Fig. 1. Visualizations in Figs. 1(a)–1(d) show that the characteristic flow regimes known to exist in the fixed-temperature case [20,44] also exist in the fixed-flux case. The scaling in Eq. (18) correctly predicts the parameters for which they occur. For small $\widetilde{\mathrm{Ra}}$ a cellular regime is observed [Fig. 1(a)], which transitions to the so-called plume regime (for $\mathrm{Pr} = 1$) as $\widetilde{\mathrm{Ra}}$ is increased [Fig. 1(b)]. At even higher supercriticality, the vertical coherence vanishes, and a state of so-called geostrophic turbulence is finally reached [Fig. 1(c)]. In case of stress-free boundary conditions a large-scale barotropic vortex forms due to an upscale transport of kinetic energy [Fig. 1(d)], an effect that is largely inhibited by no-slip boundaries.

A more quantitative comparison is given in Figs. 1(e)–1(h), where barotropic and baroclinic kinetic energy spectra are compared for different boundary conditions. In all cases, the spectra are nearly indistinguishable for both thermal boundary conditions, revealing that the scaling in Eq. (18) indeed guarantees similar bulk dynamics in all cases shown. This is the case both for stress-free, but also for no-slip boundaries. Additional simulations covering Rayleigh numbers up to $\widetilde{\mathrm{Ra}}_{FT} = 70$ (with values for $\widetilde{\mathrm{Ra}}_{FF}$ determined from Eq. (18)) all show the same behavior, demonstrating that the results are robust in the investigated Rayleigh number range. Increasing the Rayleigh number further would weaken the rotational influence successively, until essentially nonrotating convective turbulence finally results. We leave an exploration of this computationally challenging dynamical regime to future studies. However, the results of Johnston and Doering [15] suggest that Eq. (18) continues to hold in this case, at least if Ra is high enough.

Interestingly, and unlike the energy spectra considered so far, the Nusselt-Rayleigh relationship can be altered substantially by the nature of the thermal boundary condition. Figures 2(a) and 2(b) show time-averaged Nusselt numbers Nu and Reynolds numbers Re for different configurations of mechanical and thermal boundary conditions as a function of $\widetilde{\mathrm{Ra}}_{FT}$. While in all cases the Reynolds number is nearly identical for both sets of thermal boundary conditions, Nusselt numbers increased by up to $\sim$10% are observed in the fixed-flux, no-slip case. To our knowledge, this effect has not been reported previously in the literature.

In order to shed light on the physics at play, we note that the Reynolds number and the vertically averaged energy spectra mainly reflect bulk properties, whereas the Nusselt number is more closely tied to boundary layer processes. While it has long been known that Ekman pumping can substantially increase the Nusselt number by causing significant advective heat transport through the thermal boundary layer, our results indicate that the effectiveness of this process strongly depends on the nature of the thermal boundary condition. For fixed-flux boundary conditions, thermal anomalies can extend all the way to the bounding surface. This increases the advective heat transport through the thermal boundary layer and therefore reduces the average temperature drop ΔT across the layer, resulting in a larger value of the Nusselt number.

Details of this mechanism are illustrated in Figs. 2(c)–2(f). The horizontally averaged temperature field is shown in Fig. 2(c). Since different scalings are used for the fixed-flux and fixed-temperature case, a meaningful comparison requires a proper rescaling. This can be achieved

TABLE I. Summary of the input and output parameters used for the nonmagnetic, rapidly rotating convection simulations. All simulations were performed with $E = 10^{-5}$ and $\Gamma = 10\,\ell_{h,c} = 1.038$ where $\ell_{h,c}$ is the critical wavelength at the onset of convection in the stress-free case. The table contains the numerical resolution as well as the mechanical (V BC) and thermal (T BC) boundary conditions. Here (SF) denotes stress-free, (NS) no-slip, (FT) fixed-temperature, and (FF) fixed-flux conditions. Depending on the thermal boundary condition used, Ra is either the fixed-temperature Rayleigh number Ra_{FT} or the fixed-flux Rayleigh number Ra_{FF}. The Prandtl number Pr was also varied. As output parameters the Reynolds number and the Nusselt number Nu, either Nu_{FT} or Nu_{FF} depending on the temperature boundary conditions, are shown.

No.	$N_x \times N_y \times N_z$	V BC	T BC	Ra	Pr	Re	Nu
1	288 × 288 × 192	SF	FT	4.64×10^7	1	56.11 ± 3.48	1.26 ± 0.03
2	288 × 288 × 192	SF	FT	9.28×10^7	1	364.21 ± 16.38	4.75 ± 0.42
3	384 × 384 × 192	SF	FT	1.39×10^8	1	1245.04 ± 15.75	10.38 ± 1.01
4	288 × 288 × 192	SF	FT	1.86×10^8	1	2000.01 ± 16.64	15.66 ± 1.28
5	384 × 384 × 192	SF	FT	2.32×10^8	1	2705.23 ± 26.03	20.34 ± 1.64
6	384 × 384 × 192	SF	FT	3.25×10^8	1	4038.66 ± 28.93	29.82 ± 2.36
7	288 × 288 × 192	SF	FF	5.84×10^7	1	56.04 ± 10.69	1.26 ± 0.21
8	288 × 288 × 192	SF	FF	4.41×10^8	1	363.48 ± 16.99	4.78 ± 0.45
9	288 × 288 × 192	SF	FF	1.44×10^9	1	1273.04 ± 16.86	10.47 ± 1.10
10	288 × 288 × 192	SF	FF	2.91×10^9	1	2028.90 ± 17.52	15.93 ± 1.59
11	384 × 384 × 192	SF	FF	4.70×10^9	1	2708.67 ± 22.18	20.75 ± 1.85
12	384 × 384 × 192	SF	FF	9.66×10^9	1	4047.99 ± 33.10	30.28 ± 2.57
13	288 × 288 × 192	NS	FT	4.17×10^7	1	85.95 ± 3.25	1.71 ± 0.05
14	288 × 288 × 192	NS	FT	4.64×10^7	1	126.94 ± 4.39	2.36 ± 0.09
15	288 × 288 × 192	NS	FT	5.57×10^7	1	215.23 ± 6.64	4.11 ± 0.21
16	288 × 288 × 192	NS	FT	6.96×10^7	1	353.60 ± 11.31	7.51 ± 0.46
17	288 × 288 × 192	NS	FT	9.28×10^7	1	556.45 ± 21.23	12.99 ± 1.04
18	288 × 288 × 192	NS	FT	1.39×10^8	1	814.28 ± 32.68	19.55 ± 1.76
19	288 × 288 × 192	NS	FT	1.86×10^8	1	975.88 ± 36.16	22.97 ± 1.84
20	384 × 384 × 192	NS	FT	2.32×10^8	1	1104.56 ± 37.38	25.37 ± 1.80
21	384 × 384 × 192	NS	FT	3.25×10^8	1	1380.66 ± 36.81	30.14 ± 1.83
22	288 × 288 × 192	NS	FF	7.12×10^7	1	86.27 ± 4.13	1.72 ± 0.01
23	288 × 288 × 192	NS	FF	1.10×10^8	1	127.56 ± 4.89	2.40 ± 0.01
24	288 × 288 × 192	NS	FF	2.29×10^8	1	216.33 ± 7.68	4.29 ± 0.04
25	288 × 288 × 192	NS	FF	5.22×10^8	1	355.51 ± 13.71	8.07 ± 0.11
26	288 × 288 × 192	NS	FF	1.20×10^9	1	560.38 ± 23.00	14.24 ± 0.29
27	288 × 288 × 192	NS	FF	2.72×10^9	1	824.74 ± 33.92	21.62 ± 0.54
28	288 × 288 × 192	NS	FF	4.26×10^9	1	984.90 ± 38.77	25.05 ± 2.49
29	384 × 384 × 192	NS	FF	5.89×10^9	1	1113.09 ± 36.28	27.42 ± 2.18
30	384 × 384 × 192	NS	FF	9.79×10^9	1	1374.05 ± 40.08	32.11 ± 2.34
31	288 × 288 × 192	NS	FT	4.64×10^7	7	20.37 ± 0.45	2.51 ± 0.07
32	288 × 288 × 192	NS	FT	9.28×10^7	7	88.42 ± 2.82	16.08 ± 1.00
33	288 × 288 × 192	NS	FT	1.39×10^8	7	141.96 ± 4.29	27.16 ± 1.62
34	288 × 288 × 192	NS	FT	1.86×10^8	7	187.38 ± 6.08	35.75 ± 2.24
35	384 × 384 × 192	NS	FT	2.32×10^8	7	226.11 ± 7.02	42.24 ± 2.48
36	384 × 384 × 192	NS	FT	3.25×10^8	7	287.68 ± 8.66	50.70 ± 2.82
37	288 × 288 × 192	NS	FF	1.17×10^8	7	20.47 ± 0.78	2.56 ± 0.12
38	288 × 288 × 192	NS	FF	1.49×10^9	7	88.42 ± 2.95	17.90 ± 1.32
39	288 × 288 × 192	NS	FF	3.78×10^9	7	141.28 ± 4.52	30.29 ± 2.21
40	288 × 288 × 192	NS	FF	6.64×10^9	7	186.35 ± 6.67	39.73 ± 3.13
41	384 × 384 × 192	NS	FF	9.80×10^9	7	224.71 ± 8.17	46.63 ± 3.65
42	384 × 384 × 192	NS	FF	1.65×10^{10}	7	287.16 ± 10.81	55.43 ± 4.40

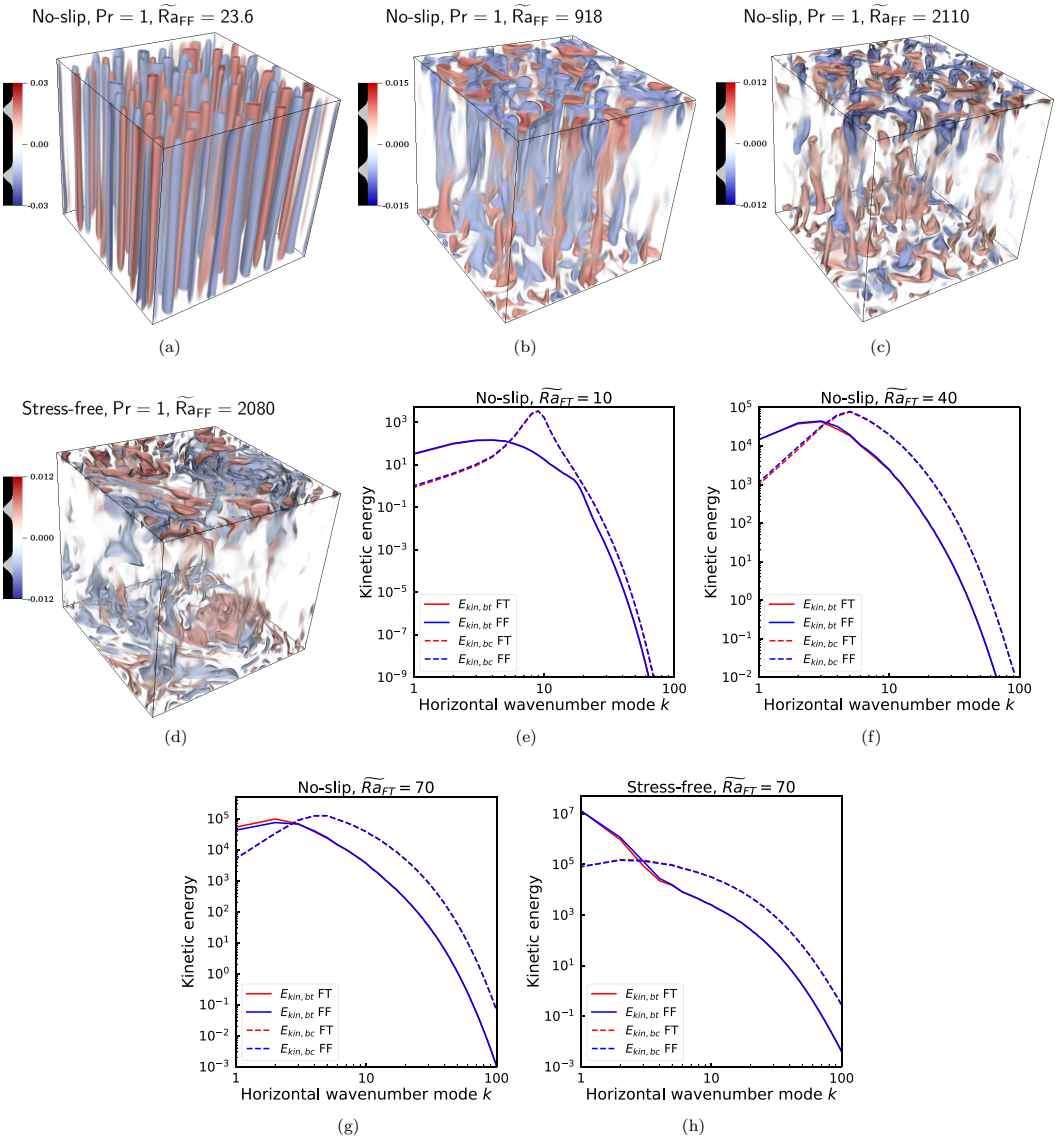

FIG. 1. Typical spatial structures observed in DNS of nonmagnetic convection at $E = 10^{-5}$ and $\mathrm{Pr} = 1$. Panels (a)–(d) show visualizations of the thermal anomaly $\theta = T - \langle T \rangle_{xy}$ obtained with an imposed heat flux. The values of $\widetilde{\mathrm{Ra}}_{FF}$ and Pr used and the mechanical boundary condition employed are indicated in each panel. Barotropic (bt) and baroclinic (bc) kinetic energy spectra are shown for the same cases in panels (e)–(h), which also include results for fixed-temperature boundary conditions. The corresponding values for $\widetilde{\mathrm{Ra}}_{FT}$ are indicated in each panel.

by using the temperature drop imposed across the layer in the fixed-temperature case as the common scaling unit for both types of boundary conditions; see Eq. (19). Figure 2(c) shows that the rescaled temperature profiles are almost indistinguishable in the bulk, whereas the thermal boundary layer structure is notably different and characterized by a smaller difference between the average bulk and boundary temperature in the fixed-flux case. This results in a reduced value of ΔT, and therefore in an increase of Nu, in the fixed-flux case.

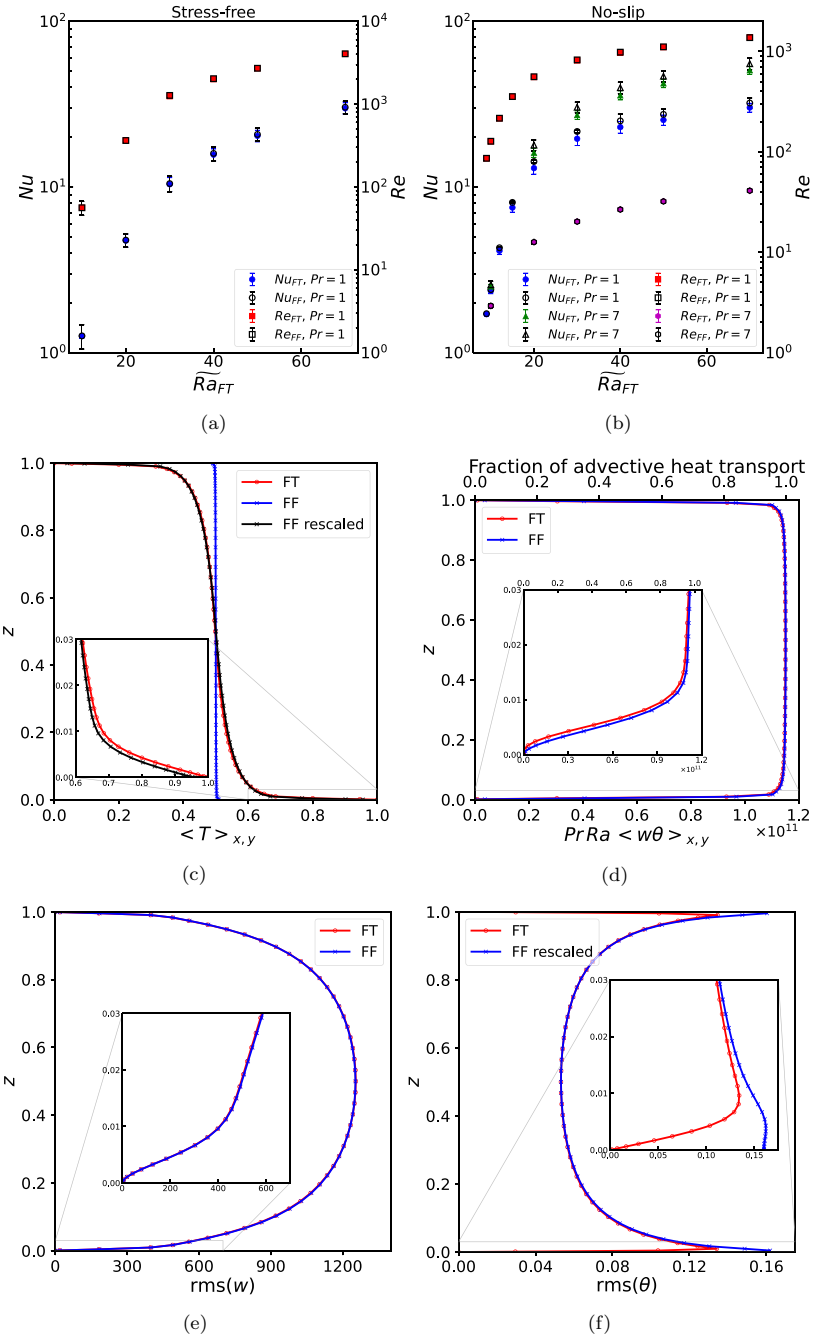

FIG. 2. The quantitative influence of the thermal boundary conditions on nonmagnetic convection at $E = 10^{-5}$. Panels (a) and (b) show Nu and Re as a function of $\widetilde{\mathrm{Ra}}$ for (a) the stress-free and (b) for no-slip boundaries. While the thermal boundary conditions appear to have an almost negligible impact for stress-free boundary conditions, Nusselt numbers deviating by up to 10% are observed in the no-slip case. Different values of Pr are shown in (b) to illustrate the Prandtl number dependence of this effect. Panels (c)–(f) illustrate the mechanism that increases the Nusselt numbers for no-slip, fixed-flux boundary conditions at $\mathrm{Pr} = 7$ and $\mathrm{Ra}_{FF} = 3550$ ($\mathrm{Ra}_{FT} = 70$).

The reason for the different thermal boundary layer structure is apparent from Fig. 2(d), which shows the fraction of the overall heat transport carried by advection. At first sight, the profiles look very similar in both cases. However, a closer inspection of the boundary layer region (inset) reveals that fixed-flux boundary conditions increase the efficiency of advection close to the boundaries. A smaller ΔT is then sufficient in the fixed-flux case to allow for the same overall heat flow.

Figures 2(e) and 2(f) show that the different efficiency of advection in the near-boundary region is not caused by a different vertical flow amplitude, but instead by stronger thermal anomalies close to the boundaries. Profiles of the RMS vertical velocity, shown in Fig. 2(e), are almost unaffected by the choice of the thermal boundary condition, both in the bulk and close to the boundary. In contrast, profiles of the lateral thermal temperature anomaly, defined as $\theta = T - \langle T \rangle_{xy}$ and shown in Fig. 2(f), are markedly different close to the boundary. While θ is forced to zero on the boundary for fixed-temperature boundary conditions, substantial thermal anomalies exist on the plates and throughout the thermal boundary layer in the fixed-flux case. This allows for a stronger advective heat transport $\langle w\theta \rangle_{xy}$ in this region, which, as already described, reduces ΔT and therefore increases Nu.

As shown earlier, the observed increase of Nu is not accompanied by noticibly larger flow velocities or an increased value of the overall Reynolds number Re. In this regard, it is important to note that the advective heat transport shown in Fig. 2(d) is directly proportional to the rate of work done by buoyancy forces. The convection is mainly driven in the bulk region, where the buoyancy power is equally strong for both sets of boundary conditions. The small differences in the buoyancy power observable within the thin thermal boundary layer have a negligible influence on the bulk dynamics.

B. Self-consistent dynamo

In this section we introduce electromagnetic induction into the model in order to investigate the effect of boundary conditions on Cartesian dynamos. Since it is impossible to cover the entire explorable, four-dimensional parameter space for all combinations of possible boundary conditions, we focus on the geophysically most relevant case of turbulent, but rotationally constrained flow, i.e., the regime of geostrophic turbulence, characterized by $\widetilde{\mathrm{Ra}} = \mathrm{Ra}E^{4/3} \gg 1$ and $\mathrm{Ro} = E\sqrt{\mathrm{Ra}/\mathrm{Pr}} \ll 1$. As described above, in the nonmagnetic case upscale kinetic energy transport is a leading order feature of this regime.

For idealized, illustrative boundary conditions (i.e., shear stress-free, fixed-temperature, and electrically perfectly conducting), dynamos within this regime have been studied by Guervilly *et al.* [34]. Guided by their work, we choose $\mathrm{Ra}_{FT} = 5.0 \times 10^8$, $E = 5 \times 10^{-6}$, $\mathrm{Pr} = 1$ and consider two values of the Roberts number, $q = 0.2$ and $q = 2.5$. The aspect ratio of the simulation domain is $\Gamma = 1$. The relevant input parameters for the dynamo simulations are presented in Table II.

In the following, we will consider mechanical boundary conditions either of stress-free or no-slip type, thermal boundary conditions which impose either a constant temperature or a constant heat flux and magnetic boundary conditions which assume either an insulating or a perfectly conducting exterior region.

1. Parameters chosen on the basis of nonmagnetic convection: Kinematic approach

In this section, we present dynamos that are started from small magnetic field perturbations superimposed onto nonmagnetic convection. Taking into account the results presented above and those presented in Stellmach *et al.* [20], Julien *et al.* [21], and Plumley *et al.* [22,23], the role of mechanical and thermal boundary conditions on the nonmagnetic base flow may be considered as reasonably well understood in the investigated parameter regime. In the case of an imposed heat flux, the Rayleigh number Ra_{FF} is chosen by the same procedure as described in Sec. III A, i.e., according to Eq. (18), where Nu_{FT} is the Nusselt number obtained for fixed-temperature boundary conditions in the nonmagnetic case. As we have shown, this guarantees that the nonmagnetic flow

TABLE II. Summary of the input parameter for the dynamo simulations. All simulations were performed with a resolution of $288 \times 288 \times 256$, $\Gamma = 1$, $E = 5 \times 10^{-6}$, and $\mathrm{Pr} = 1$. The table displays the mechanical boundary conditions (V BC) which are either stress-free (SF) or no-slip (NS), the thermal boundary conditions (T BC) which are either fixed-temperature (FT) or fixed-flux (FF), and the magnetic boundary conditions (MAG BC) which are either perfectly conducting (PERF) or insulating (INSU). Depending on the temperature boundary condition Ra is either the fixed-temperature Rayleigh number Ra_{FT} or the flux Rayleigh number Ra_{FF}. The Roberts number q is also shown. Cases with an asterisk denote the runs where the flux Rayleigh number was chosen by the "kinematic approach."

No.	V BC	T BC	MAG BC	Ra	q
1	SF	FT	PERF	5.00×10^{8}	2.5
2	SF	FT	PERF	5.00×10^{8}	0.2
3	SF	FT	INSU	5.00×10^{8}	2.5
4	SF	FT	INSU	5.00×10^{8}	0.2
5*	SF	FF	INSU	8.52×10^{9}	2.5
6	SF	FF	INSU	1.05×10^{10}	2.5
7*	SF	FF	INSU	8.52×10^{9}	0.2
8	SF	FF	INSU	9.50×10^{9}	0.2
9	NS	FT	PERF	5.00×10^{8}	2.5
10	NS	FT	INSU	5.00×10^{8}	2.5
11*	NS	FF	INSU	1.27×10^{10}	2.5
12	NS	FF	INSU	1.50×10^{10}	2.5
13*	NS	FF	INSU	1.27×10^{10}	0.2

exhibits a similar flow structure in the bulk for both types of thermal boundary conditions if all other boundary conditions are identical, and that it is characterized by the same magnetic Reynolds number. The resulting kinematic dynamos are therefore almost indistinguishable for both types of thermal boundary conditions.

Figure 3 illustrates the topology of the flow and the magnetic field in the saturated state. For simplicity, and to keep the paper within reasonable bounds, results are displayed only for fixed-flux thermal boundary conditions and for an electrically insulating exterior region, a case that to our knowledge has not been discussed in the literature before. Similar plots for other thermal and magnetic boundary conditions turn out to be visually indistinguishable from the ones shown, and the subtle differences that arise are better discussed in terms of other quantities than chosen in the figure.

The most striking feature of the graphs shown in Fig. 3 is the massive effect of the mechanical boundary condition on the type of dynamo that is established. In particular, small-scale magnetic fields are always dominant for rigid boundary conditions, in contrast to the stress-free case, where large-scale fields and flows are found at small enough Roberts number. In fact, in the case of stress-free boundary conditions, two types of dynamos are observed, in line with previous results by Guervilly *et al.* [34] for the more idealized illustrative boundary conditions. For a high Roberts number, $q = 2.5$, the generated magnetic field destroys the large-scale barotropic vortex that forms in the nonmagnetic case, resulting in a small-scale dynamo [cf. Figs. 3(a) and 3(b)]. If the Roberts number is reduced to $q = 0.2$, the barotropic vortex is not completely destroyed and a so-called "large-scale vortex (LSV) dynamo" forms [cf. Figs. 3(c) and and 3(d)]. Here the magnetic field is mainly induced by the large-scale flow and therefore has similar spacial scales. For these dynamos, the vortex persists in an oscillatory manner, depending on the current strength of the magnetic field. Even though both the thermal and magnetic boundary conditions are different from the simple ones employed by Guervilly *et al.* [34], the leading order dynamics follows their description precisely. We therefore do not present a more detailed discussion here, but instead refer the reader to the publications of Guervilly *et al.* [34] and Guervilly *et al.* [49].

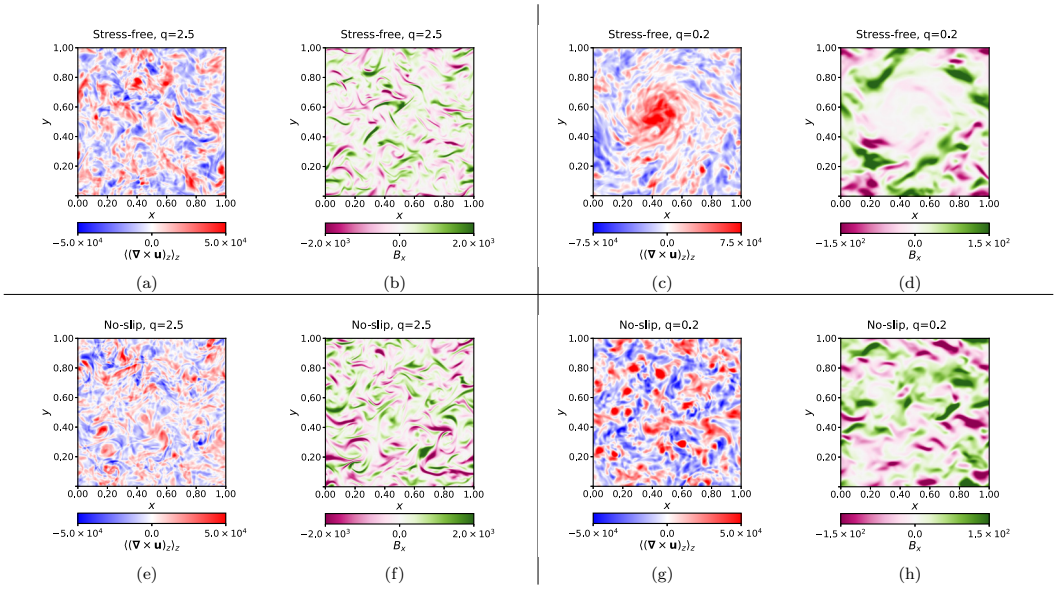

FIG. 3. Typical flow and magnetic field structures observed in DNS of Cartesian dynamos at $E = 5 \times 10^{-6}$, $\mathrm{Pr} = 1$, and $\mathrm{Ra}_{FT} = 5.0 \times 10^8$ (corresponding to $\mathrm{Ra}_{FF} = 8.52 \times 10^9$ for stress-free and $\mathrm{Ra}_{FF} = 1.27 \times 10^{10}$ for no-slip boundary conditions) with an imposed heat flux and an electrically insulating exterior region. Panels (a), (c), (e), and (g) show the vertically averaged vertical vorticity $\langle(\boldsymbol{\nabla} \times \boldsymbol{u})_z\rangle_z$, whereas panels (b), (d), (f), and (h) show B_x at a system height of $z = 0.2$. The value for q and the mechanical boundary conditions used are indicated in each panel.

The presence of no-slip boundaries changes the dynamics completely. Here the resulting dynamos do not generate coherent large-scale magnetic fields. As in the nonmagnetic case, the formation of stable, large-scale vortex is inhibited, and the flow is dominated by turbulent, plume-like structures on small spatial scales. The imprint of these flow structures is clearly visible in the magnetic field, which exhibits similar spatial scales. As expected, larger magnetic field gradients occur for $q = 2.5$, while for $q = 0.2$, the increased diffusion smoothes out the magnetic field structures and also decreases the field strength, such that the magnetic energy becomes too low to strongly affect the flow dynamics. In summary, by suppressing the formation of a large-scale vortex, the no-slip mechanical boundary condition eliminates the ability of the system to generate a large-scale magnetic field in this turbulent regime.

While these first-order results may not seem very surprising in the light of our findings for the nonmagnetic case, it is important to point out that the thermal boundary conditions have little effect on the dynamics of the bulk flow, and in particular we will show later on that their influence on the flow scales is almost completely negligible, contrary to what might have been expected on the basis of the arguments presented by Hori *et al.* [47]. The influence of the magnetic boundary conditions is more complicated, and we will provide a detailed discussion below. However, before we dive into more quantitative results, we first point out a weakness of the present choice of the control parameters for fixed-flux boundary conditions.

2. The "saturated" approach of choosing flux Rayleigh numbers

In all cases shown above, the flux Rayleigh number Ra_{FF} was chosen to guarantee almost identical nonmagnetic flows for both types of thermal boundary conditions. Because this choice leads to a similar kinematic growth phase of the dynamo, we call it the *kinematic approach for choosing* Ra_{FF}. While this procedure guarantees comparable conditions in the early stage of the

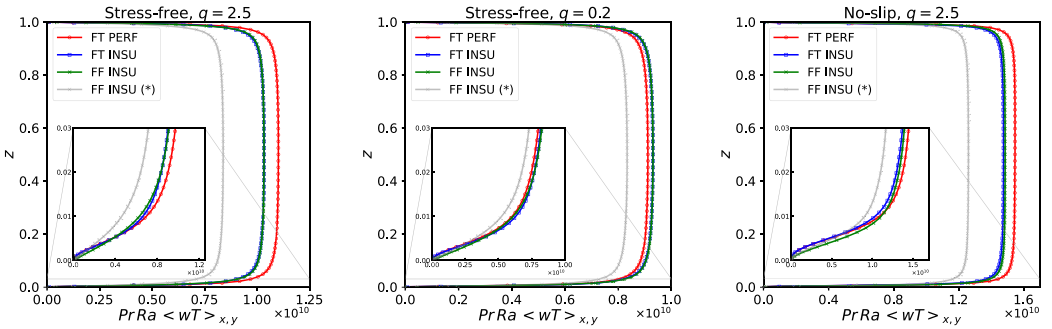

FIG. 4. Buoyancy power profiles for the three different types of dynamos considered in this study with different combinations of boundary conditions. The value of q and the mechanical boundary condition used are indicated in each panel. The cases represented by a gray line are those where Ra_{FT} was rescaled to Ra_{FF} by Eq. (18) with the Nusselt number obtained from the nonmagnetic solution (kinematic approach). For reasons of illustration, only every fourth point is displayed in the profiles, except for the inset.

simulation, differences in the overall energy balance become unavoidable once the magnetic energy exceeds a certain amplitude. In the fixed-temperature case, a sufficiently strong magnetic field affects the convective flow, which typically changes the heat flux through the boundaries. A similar adjustment is not possible under fixed-flux conditions, where the amount of heat forced through the system is held at the nonmagnetic level for all times. Except in cases where the magnetic field saturates at a very low level, we can therefore not expect any kind of quantitative agreement between fixed-flux and fixed-temperature cases if we follow the kinematic approach.

An obvious alternative is to compute the fixed-flux Rayleigh number Ra_{FF} by determining Nu_{FT} in Eq. (18) from saturated dynamo simulations. As before, these use fixed-temperature boundary conditions, but are otherwise set up identically, including the choice of the magnetic boundary condition. While this approach of determining Ra_{FF} inevitably causes differences during the kinematic growth phase, the amount of heat channeled through both systems per time unit becomes identical in the saturated dynamo state, resulting, as we demonstrate below, in quantitatively almost identical kinetic energy production characteristics. As the Nusselt number for the saturated fixed-temperature dynamo needs to be known to determine Ra_{FF}, we call this the *saturated approach of choosing* Ra_{FF}.

In order to illustrate the differences between both strategies quantitatively, Fig. 4 compares the time-averaged amount of power released by the buoyancy forces for both approaches as a function of height. As evident from the figure, the modified approach guarantees that the flow is driven equally strong almost everywhere in both cases (i.e., the blue and green lines in the figure almost fall on top of each other). Notable differences occur only within the boundary layers, which has little impact on the overall dynamics because the kinetic energy production is small in these regions anyway. These small differences are unavoidable because the power released by the buoyancy forces is directly proportional to the advective heat flux, which we know to be increased close to the boundary for fixed-flux conditions, especially if Ekman pumping comes into play (cf. Sec. III A). If we use the nonmagnetic Nusselt number to determine Ra_{FF} (gray line), the convective driving is much weaker everywhere. Quantitatively, this effect even supersedes the consequences of changing the magnetic boundary condition from insulating to perfectly conducting (red line). It is therefore clear that detailed, quantitative comparisons of flow and field characteristics are much easier to interpret if we choose the fixed-flux Rayleigh number in a "saturated" fashion. In the following, we therefore always take this approach unless stated otherwise, i.e., we compute Ra_{FF} by using Nusselt numbers Nu_{FT} from saturated dynamos and not from nonmagnetic convection. We emphasize, however, that this is mainly important for quantitative comparisons. The leading order features of the solution, as illustrated in Fig. 3, remain unaffected.

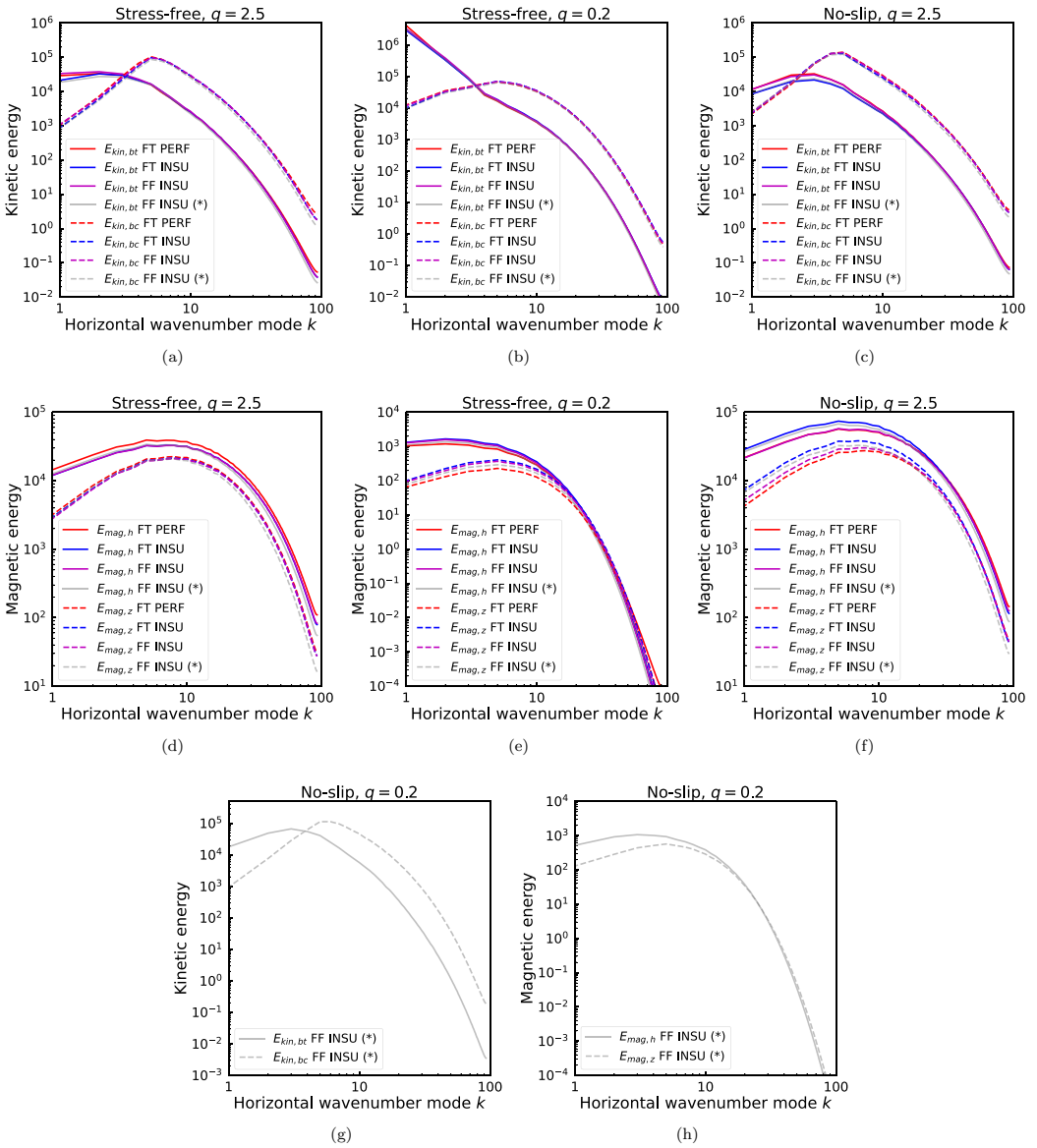

FIG. 5. Kinetic and magnetic energy spectra obtained from DNS of dynamos at $E = 5 \times 10^{-6}$, $\mathrm{Pr} = 1$, and $\mathrm{Ra}_{FT} = 5 \times 10^8$ for different combinations of boundary conditions. Panels (a)–(c) and (g) show the horizontal kinetic energy spectra divided in its barotropic and baroclinic components, whereas panels (d)–(f) and (h) show the magnetic energy divided in its horizontal and vertical components. The value of q and the mechanical boundary condition used are indicated in each panel. The spectra in panels (g) and (h) show only one combination of boundary conditions due to high computational costs of this dynamo solution.

3. Flow and magnetic field spectra

A good quantitative measure characterizing the solution structure is provided by kinetic and magnetic energy spectra, which are shown for different sets of boundary conditions in Fig. 5. Again, the kinetic energy has been decomposed into barotropic and baroclinic parts, whereas the magnetic energy is shown separately for the horizontal and vertical components. We note that

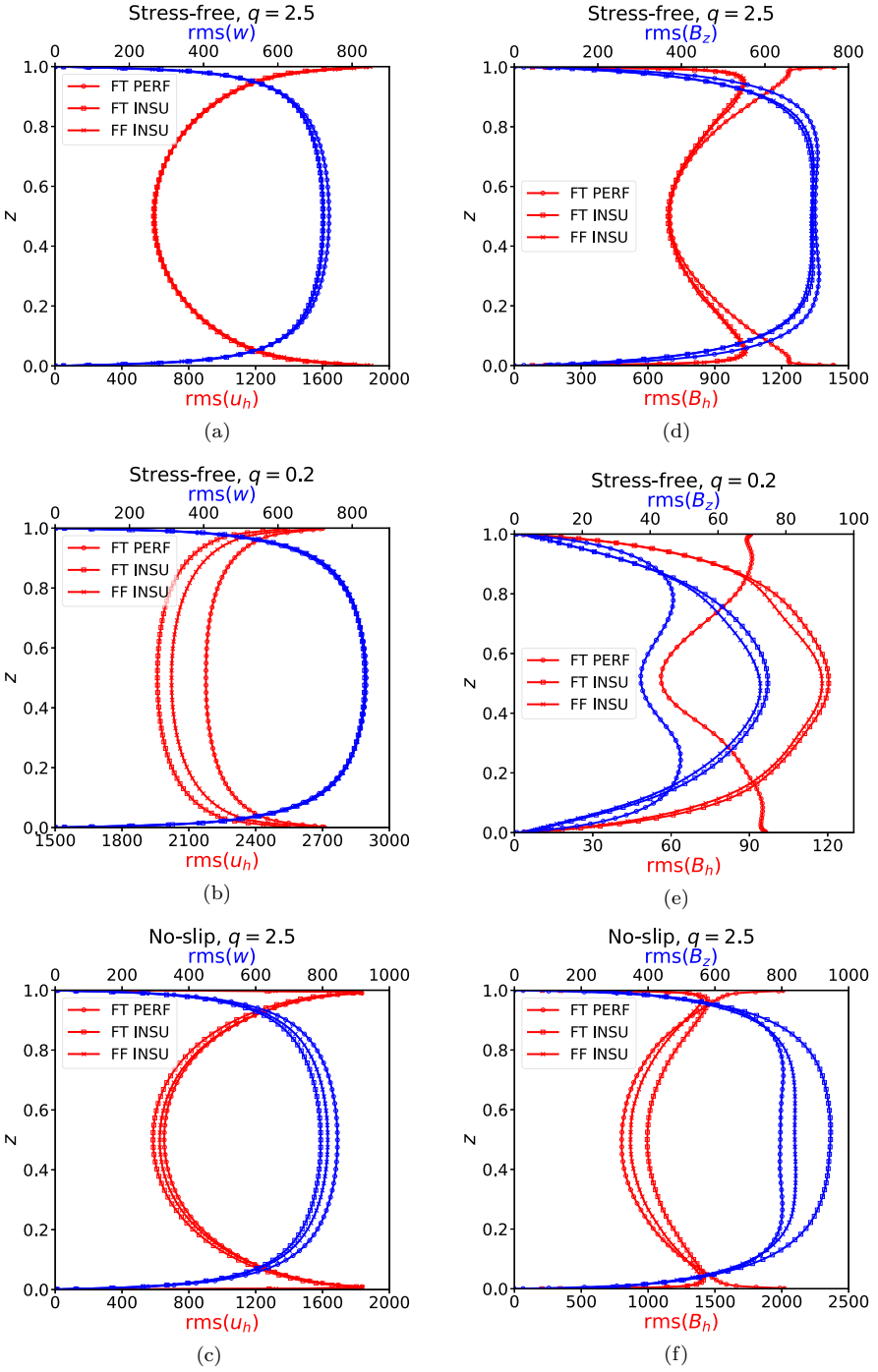

FIG. 6. Profiles of the root-mean-square (rms) velocity and magnetic field components for the different dynamo cases. Different configurations of the temperature and magnetic boundary conditions are considered. Panels (a) and (d) show the case with stress-free boundary conditions and $q = 2.5$, whereas panels (b) and (e) show the case for the LSV dynamo with stress-free boundary conditions and $q = 0.2$. Panels (c) and (f) show the dynamo with no-slip boundary conditions and $q = 2.5$. For reasons of illustration, only every fourth point is displayed in the profiles.

determining time-averaged spectra such as the ones shown here is much more demanding than in the nonmagnetic case because the time series in the dynamo case are characterized by the presence of much slower modes, which requires the computation of longer time series in order to get reasonable statistics. Furthermore, the Alfvén wave speed adds a further restriction on the time step length, especially for no-slip, electrically insulating boundary conditions. These require a small vertical grid spacing within the Ekman layer, where the insulating exterior simultaneously allows for considerable vertical magnetic field components. Combined, both lead to severe time step restrictions. In order to keep the computational costs within reasonable bounds, we performed a systematic comparison of only thermal and magnetic boundary conditions for $q = 2.5$ in the no-slip case. For $q = 0.2$, only one simulation was performed which employs fixed-flux and electrically insulating boundaries and follows the "kinematic approach" for choosing the flux Rayleigh number. For stress-free boundary conditions, two levels of magnetic diffusion, characterized by $q = 0.2$ and $q = 2.5$, are fully explored.

Figure 5 illustrates the properties of the dynamos that we already discussed qualitatively in the context of Fig. 3. The presence of a large-scale barotropic vortex, as well as its suppression by the magnetic field and/or the mechanical boundary conditions, is clearly visible. Perhaps the most striking feature of the spectra shown in Fig. 5, however, is their similarity for all kinds of thermal and electrical boundary conditions considered. This is especially evident for the kinetic energy spectra, where the different curves are almost indistinguishable. Moderate differences are encountered in cases where the flux Rayleigh number is chosen by the *kinematic* approach, where the convection is typically driven less vigorously (cf. Fig. 4). The reduced kinetic energy input is reflected by a slightly less turbulent flow, resulting in less kinetic energy in the small-scale eddies, especially in the baroclinic part of the spectrum (gray curves). Furthermore, all curves deviate slightly for the large-scale, barotropic modes. We emphasize that these flow components evolve on very long temporal scales, and we do not claim that our times series are long enough to provide accurate temporal averages for these slow modes. Instead, the apparent differences in the energy of the low wave number, barotropic modes may well be caused by imperfect temporal averaging. This interpretation is also supported by the fact that the parts of the spectra which represent faster evolving modes (i.e., the baroclinic kinetic energy spectra, and the higher orders of the barotropic spectrum) agree almost perfectly for all boundary conditions employing the saturated approach.

An important result illustrated by the kinetic energy spectra is that the thermal boundary condition has an almost negligible influence on the flow scales. Different from observations made in spherical shell simulations [46–48], fixed-flux conditions do not allow for a noticeable increase in the size of the eddies. A possible explanation is that thermal winds are of major importance in the spherical case for flux boundary conditions and strongly affect the magnetic field generation process [48]. Furthermore, our dynamos are in a strongly nonlinear regime and arguments based on linear stability theory, as put forth in Sakuraba and Roberts [46], Hori *et al.* [47], and Matsui *et al.* [48], may therefore not be applicable.

In case of the magnetic energy, all spectra are still very similar, but the agreement for different types of thermal and magnetic boundary conditions is less perfect than for the kinetic energy. Especially large differences are found for no-slip mechanical boundary conditions, an effect we currently do not fully understand. A further interesting aspect of the magnetic spectra is that, upon close inspection, they seem to reveal a systematic effect of the magnetic boundary condition. This will become more evident if the vertical solution structure is studied, as done in the next section.

4. Vertical structure of the solution

The energy spectra discussed so far were presented using a logarithmic scale, which reveals their characteristics over a large dynamical range, but also masks small-amplitude variations. In order to provide a closer look, and also to shed light on the vertical structure of the solution, we present profiles of horizontal and vertical flow and magnetic field components in Fig. 6.

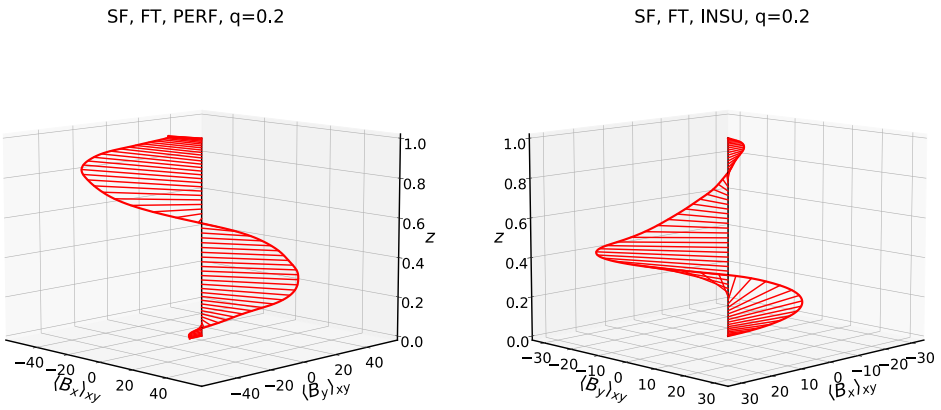

(a) (b)

FIG. 7. Snapshots of the mean magnetic field structure along the vertical axis of the LSV dynamo for different magnetic boundary conditions.

It now becomes apparent that small differences in the flow amplitude indeed exist, but that the vertical structure is very similar in all cases. This is not true, however, for the magnetic field, whose topology strongly depends on the electric boundary conditions, in agreement with analytical arguments put forth by Jones and Roberts [27]. The shape of the profiles differs in the bulk as well as close to the boundaries. Interestingly, perfectly conducting boundary conditions, which are usually chosen both for simplicity and numerical convenience, lead to a strong buildup of field close to the perfectly conducting surfaces, especially in the case with less magnetic diffusion, $q = 2.5$. This results in a thin layer of intense horizontal field, an effect mentioned briefly by St. Pierre [29] and in the study for nonrotating plane layer dynamos by Thelen and Cattaneo [50]. This is undesirable from a numerical point of view, and adds complexity to the dynamics, contrary to what one usually hopes to achieve by using illustrative boundary conditions.

To further exemplify the influence of the magnetic boundary conditions, Fig. 7 shows the vertical structure of the horizontal mean magnetic field $\langle B_x \mathbf{e}_\mathbf{x} + B_y \mathbf{e}_y \rangle_{xy}$ for the LSV dynamo under different magnetic boundary conditions. As already shown for the perfectly conducting case by Guervilly *et al.* [49], the LSV dynamo generates a mean field with a spiral structure, similar to the mean fields observed close to convective onset [30]. It is interesting to compare the mean field topology for different magnetic boundary conditions. While the mean field is forced to zero at the edge of the layer if the exterior region is electrically insulating, it reaches a considerable strength on a perfectly conducting boundary surface. Furthermore, as pointed out by Jones and Roberts [27], perfectly conducting boundaries force the vertically integrated mean field to vanish, which results in a pronounced antisymmetry with respect to the midplane in our simulations. In contrast, a net mean magnetic field becomes possible if the exterior region is insulating, and indeed high mean field amplitudes are observed at midlayer in our simulations. The high Roberts number dynamos ($q = 2.5$, not shown in the figure) exhibit much more incoherent mean fields dominated by smaller scales.

In summary, we conclude that while the magnetic boundary conditions have only a moderate effect on the horizontal kinetic and magnetic energy distribution, they heavily constrain the vertical magnetic field topology and therefore the entire dynamo solutions.

In contrast to the magnetic boundary conditions, the effects of the thermal boundary conditions on the vertical solution structure is more gradual. While some quantitative differences are clearly observed, the thermal boundary condition does not seem to have an impact on the overall vertical

solution topology. This again adds support to the conclusion that the choice of the thermal boundary condition has a very limited impact on turbulent Cartesian dynamos.

IV. CONCLUSIONS AND DISCUSSION

The main goal of this study is to shed light on the role boundary conditions play in turbulent dynamos of Childress-Soward type. With most of the existing studies [29–34,49] focusing on idealized, simple boundary conditions, our results fill a gap within the existing literature. The simple geometrical configuration provides an ideal test bed for studying boundary-induced effects, building on the large amount of knowledge that has been collected in the context of rotating and nonrotating Rayleigh-Bénard convection over the last few decades.

One question that has remained open in the field of rotating Rayleigh-Bénard convection concerns the role of the thermal boundary condition. While many previous studies have focused on the impact of the mechanical properties of the boundaries, the dynamical effects caused by their thermal properties have received little attention so far. We thus investigated this issue, both to complete the existing literature but also to lay the necessary groundwork for our dynamo study. Our most striking result concerns the Nusselt-Rayleigh relationship which quantifies the efficiency of the overall heat transfer. We find that in the experimentally relevant case of no-slip boundaries, the Nusselt number is increased significantly if fixed-flux boundary conditions are used instead of fixed-temperature ones. This effect can be explained by an interplay between Ekman pumping and the internal structure of the thermal boundary layer, which is sensitive to the thermal boundary condition applied. This phenomenon, which is clearly of interest to experimentalists, theoreticians, and geophysicists alike, has to our knowledge not been reported previously.

While the Nusselt-Rayleigh relationship in rotating plane layer convection clearly differs for fixed-flux and fixed-temperature boundary conditions, we find that the bulk dynamics remains largely unaffected. The observed change in the Nusselt number is caused purely by localized boundary layer processes and not by a leading-order adjustment of the bulk dynamics. As a result, the same flow regimes that had been reported for the fixed-temperature case [20,44,45] are also found for fixed-flux conditions, with the flow amplitude being identical in both cases. This finding is in line with with asymptotic predictions [43] for stress-free mechanical boundary conditions. For the dynamo case this implies that during the kinematic growth phase, the field generation process remains unaffected by the nature of the thermal boundary condition.

Equipped with previous results [20–22,24] on the influence of mechanical boundary conditions on rotating Rayleigh-Bénard convection and our results concerning the thermal boundary conditions, we turned our attention to the dynamo case, focusing on the geophysically most relevant scenario in which the flow is characterized by geostrophic turbulence [49]. Simulations with different combinations of mechanical, thermal and magnetic boundary conditions were carried out and the results were compared.

As expected, the velocity boundary conditions have a major effect on the resulting dynamos. For no-slip boundary conditions, Ekman friction diminishes the efficiency of upscale kinetic energy transport [20,22,24], such that no coherent large-scale vortices form in our simulations. In contrast, for stress-free mechanical boundaries, the large-scale vortex dynamos described in [49] are observed for sufficiently small Roberts number. The mechanical boundary conditions thus control whether intense large-scale fields and flows are generated within the system. This behavior is found for all combinations of mechanical, magnetic, and thermal boundary conditions considered in our study. An open question in this respect is whether more extreme control parameters, in particular smaller Ekman numbers paired with larger supercriticality, would allow for large-scale vortex dynamos also in the no-slip case. Indeed, recent numerical [53] and laboratory studies [54] in the nonmagnetic case point into this direction. An investigation of this question is left for future studies as massive computational resources would be needed to carry out the respective simulations.

We also studied the effect of the thermal boundary conditions on the dynamo states. An important question arising in this context is how the Rayleigh numbers can be chosen to allow for

a meaningful, direct and quantitative comparison of the fixed-temperature case with the fixed-flux case. A naive approach is to choose them in a way that guarantees the same bulk dynamics and flow amplitude as in the nonmagnetic case. While this leads to the same system behavior during the kinematic growth phase, our results clearly show that the similarity is lost as soon as the magnetic energy becomes significant. For fixed-temperature boundary conditions, the heat transport across the layer adjusts to the dynamical changes caused by the Lorentz forces, whereas a similar adjustment is impossible for an externally imposed heat flux. As a result, both systems are driven with different strength, and a quantitative agreement can never be reached.

In contrast, if both Rayleigh numbers are chosen such that the same amount of heat is channeled through the layer in the saturated dynamo state, very similar solutions are obtained, even on a quantitative level. The only exception is the near-wall behavior of the temperature field and the associated shift in the Nusselt number already found in the nonmagnetic case. Interestingly, we see no evidence for an increase of the spatial scales for fixed-flux conditions, as may be anticipated from previous results in spherical geometry [46,47] and from simple arguments based on linear stability analysis for an imposed vertical field [47]. Clearly, the magnetic fields generated by our dynamos are much more complicated, and the conditions are turbulent rather than weakly supercritical. We conclude that if the Rayleigh numbers are chosen in a sensible way, the thermal boundary conditions are of secondary importance for studies of turbulent, Cartesian dynamos. Whether this also holds in weakly supercritical regimes needs to be investigated in future studies. While interesting from a theoretical point of view, this question probably has little geophysical significance.

Finally, we also studied the effect of choosing either an electrically insulating exterior region or a perfectly conducting one. A key result is that both the topology of the magnetic field and its near-wall behavior depend strongly on the choice of the magnetic boundary condition. In particular, a strong buildup of magnetic field in the outer part of the fluid layer is found for perfectly conducting boundaries, which may be attributed to the fact that the field remains trapped within the fluid [29,50]. In contrast, the near-wall region hosts much weaker fields for an electrically insulating exterior region. For large magnetic Reynolds numbers we see that very thin layers of intense horizontal field form adjacent to perfectly conducting boundaries. This complicates the dynamics and is undesirable from a numerical point of view, as the thin magnetic layers need to be resolved properly. The computational and conceptional simplifications one hopes to achieve by assuming a perfectly conducting exterior may therefore not be reached in practice. Interestingly, the horizontal distribution of both kinetic and magnetic energy is not strongly affected by the choice of the magnetic boundary condition in our simulations. Thus, for studies not focusing specifically on details of the magnetic field topology, the exact nature of the exterior region seems to be of secondary importance in the investigated parameter regime. However, we caution that this conclusion should not be generalized to other dynamical regimes, especially in view of the recent results by Bushby *et al.* [51].

Our study has focused entirely on simple boundary conditions representing extreme end-member cases. It would be interesting to look at geophysically motivated special examples, like mechanically "rough" boundaries, thermal boundary conditions as they arise at a freezing inner core interface, or special magnetic boundary conditions. An interesting example for the latter arises in planetary bodies like Mercury or Ganymede which are influenced by strong external magnetic fields having their origin in the intense solar wind or Jupiter's magnetosphere, respectively. The long-period external magnetic field components diffusive down to the planetary core, where they need to be taken into account. In dynamo simulations, this is usually implemented by imposing appropriate magnetic boundary conditions on the core-mantle boundary [55–59].

An interesting extension of our study would be to conduct similar simulations in spherical geometry, especially with respect to the thermal boundary conditions. It remains unclear whether our findings carry over to this case, because geometrical differences and possible thermal wind effects may significantly complicate the dynamics. However, a recent study by Clarté *et al.* [60] gives a first hint about the validity of our findings in spherical geometry regarding the thermal boundary

conditions. Future advances in this direction may use our Cartesian results as a reference point for quantifying the influence of the spherical geometry.

ACKNOWLEDGMENTS

We greatly thank K.-H. Glassmeier for a fruitful discussion and helpful suggestions regarding the contents of this work. We thank two anonymous reviewers for helpful comments that improved our manuscript. The authors gratefully acknowledge the Gauss Centre for Supercomputing e.V. [61] for funding this project by providing computing time through the John von Neumann Institute for Computing (NIC) on the GCS Supercomputer JUWELS [62] at Jülich Supercomputing Centre (JSC). We also gratefully acknowledge the user council of the Phoenix supercomputer at TU Braunschweig for providing computing time on the cluster. D.H. was supported by the German Ministerium für Wirtschaft und Energie and the German Zentrum für Luft- und Raumfahrt under Contracts No. 50QW1501 and 50QJ1501. Three-dimensional visualizations were produced using VisIt [63], whereas other figures were generated with Matplotlib [64].

[1] S. Childress and A. M. Soward, Convection-Driven Hydromagnetic Dynamo, Phys. Rev. Lett. **29**, 837 (1972).
[2] G. Ahlers, S. Grossmann, and D. Lohse, Heat transfer and large scale dynamics in turbulent Rayleigh-Bénard convection, Rev. Mod. Phys. **81**, 503 (2009).
[3] W. V. R. Malkus, The heat transport and spectrum of thermal turbulence, Proc. R. Soc. London A **225**, 196 (1954).
[4] C. H. B. Priestley, *Turbulent Transfer in the Lower Atmosphere* (University of Chicago Press, Chicago, 1959).
[5] B. Castaing, G. Gunaratne, F. Heslot, L. Kadanoff, A. Libchaber, S. Thomae, X.-Z. Wu, S. Zaleski, and G. Zanetti, Scaling of hard thermal turbulence in Rayleigh-Bénard convection, J. Fluid Mech. **204**, 1 (1989).
[6] B. I. Shraiman and E. D. Siggia, Heat transport in high-Rayleigh-number convection, Phys. Rev. A **42**, 3650 (1990).
[7] S. Grossmann and D. Lohse, Scaling in thermal convection: A unifying theory, J. Fluid Mech. **407**, 27 (2000).
[8] E. P. van der Poel, R. Ostilla-Mónico, R. Verzicco, and D. Lohse, Effect of velocity boundary conditions on the heat transfer and flow topology in two-dimensional Rayleigh-Bénard convection, Phys. Rev. E **90**, 013017 (2014).
[9] S.-D. Huang, F. Wang, H.-D. Xi, and K.-Q. Xia, Comparative Experimental Study of Fixed Temperature and Fixed Heat Flux Boundary Conditions in Turbulent Thermal Convection, Phys. Rev. Lett. **115**, 154502 (2015).
[10] A. Pandey, J. D. Scheel, and J. Schumacher, Turbulent superstructures in Rayleigh-Bénard convection, Nat. Commun. **9**, 1 (2018).
[11] E. A. Spiegel, Convection in stars I. Basic Boussinesq convection, Annu. Rev. Astron. Astrophys. **9**, 323 (1971).
[12] R. H. Kraichnan, Turbulent thermal convection at arbitrary Prandtl number, Phys. Fluids **5**, 1374 (1962).
[13] L. Skrbek and P. Urban, Has the ultimate state of turbulent thermal convection been observed? J. Fluid Mech. **785**, 270 (2015).
[14] C. R. Doering, S. Toppaladoddi, and J. S. Wettlaufer, Absence of Evidence for the Ultimate Regime in Two-Dimensional Rayleigh-Bénard Convection, Phys. Rev. Lett. **123**, 259401 (2019).
[15] H. Johnston and C. R. Doering, Comparison of Turbulent Thermal Convection between Conditions of Constant Temperature and Constant Flux, Phys. Rev. Lett. **102**, 064501 (2009).
[16] K. Petschel, S. Stellmach, M. Wilczek, J. Lülff, and U. Hansen, Dissipation Layers in Rayleigh-Bénard Convection: A Unifying View, Phys. Rev. Lett. **110**, 114502 (2013).

[17] E. M. King, S. Stellmach, J. Noir, U. Hansen, and J. M. Aurnou, Boundary layer control of rotating convection systems, Nature (London) **457**, 301 (2009).
[18] K. Julien, E. Knobloch, A. M. Rubio, and G. M. Vasil, Heat Transport in Low-Rossby-Number Rayleigh-Bénard Convection, Phys. Rev. Lett. **109**, 254503 (2012).
[19] E. M. King, S. Stellmach, and J. M. Aurnou, Heat transfer by rapidly rotating Rayleigh-Bénard convection, J. Fluid Mech. **691**, 568 (2012).
[20] S. Stellmach, M. Lischper, K. Julien, G. Vasil, J. S. Cheng, A. Ribeiro, E. M. King, and J. M. Aurnou, Approaching the Asymptotic Regime of Rapidly Rotating Convection: Boundary Layers versus Interior Dynamics, Phys. Rev. Lett. **113**, 254501 (2014).
[21] K. Julien, J. M. Aurnou, M. A. Calkins, E. Knobloch, P. Marti, S. Stellmach, and G. M. Vasil, A nonlinear model for rotationally constrained convection with Ekman pumping, J. Fluid Mech. **798**, 50 (2016).
[22] M. Plumley, K. Julien, P. Marti, and S. Stellmach, The effects of Ekman pumping on quasi-geostrophic Rayleigh–Bénard convection, J. Fluid Mech. **803**, 51 (2016).
[23] M. Plumley, K. Julien, P. Marti, and S. Stellmach, Sensitivity of rapidly rotating Rayleigh-Bénard convection to Ekman pumping, Phys. Rev. Fluids **2**, 094801 (2017).
[24] R. P. J. Kunnen, R. Ostilla-Mónico, E. P. van der Poel, R. Verzicco, and D. Lohse, Transition to geostrophic convection: The role of the boundary conditions, J. Fluid Mech. **799**, 413 (2016).
[25] C. Guervilly, D. W. Hughes, and C. A. Jones, Large-scale vortices in rapidly rotating Rayleigh–Bénard convection, J. Fluid Mech. **758**, 407 (2014).
[26] P. H. Roberts and C. A. Jones, The onset of magnetoconvection at large Prandtl number in a rotating layer I. Finite magnetic diffusion, Geophys. Astrophys. Fluid Dyn. **92**, 289 (2000).
[27] C. A. Jones and P. H. Roberts, Convection-driven dynamos in a rotating plane layer, J. Fluid Mech. **404**, 311 (2000).
[28] J. Rotvig and C. A. Jones, Rotating convection-driven dynamos at low Ekman number, Phys. Rev. E **66**, 056308 (2002).
[29] M. G. St. Pierre, The strong field branch of the Childress-Soward dynamo. in *Solar and Planetary Dynamos*, edited by M. R. E. Proctor, P. C. Matthews, and A. M. Rucklidge (Cambridge University Press, Cambridge, 1993), pp. 295–302.
[30] S. Stellmach and U. Hansen, Cartesian convection driven dynamos at low Ekman number, Phys. Rev. E **70**, 056312 (2004).
[31] F. Cattaneo and D. W. Hughes, Dynamo action in a rotating convective layer, J. Fluid Mech. **553**, 401 (2006).
[32] D. W. Hughes and F. Cattaneo, The alpha-effect in rotating convection: Size matters, J. Fluid Mech. **594**, 445 (2008).
[33] A. Tilgner, Transitions in Rapidly Rotating Convection Driven Dynamos, Phys. Rev. Lett. **109**, 248501 (2012).
[34] C. Guervilly, D. W. Hughes, and C. A. Jones, Generation of magnetic fields by large-scale vortices in rotating convection, Phys. Rev. E **91**, 041001(R) (2015).
[35] D. W. Hughes and F. Cattaneo, Strong-field dynamo action in rapidly rotating convection with no inertia, Phys. Rev. E **93**, 061101(R) (2016).
[36] F. Cattaneo and D. W. Hughes, Dynamo action in rapidly rotating Rayleigh-Bénard convection at infinite Prandtl number, J. Fluid Mech. **825**, 385 (2017).
[37] D. W. Hughes and F. Cattaneo, Force balance in convectively driven dynamos with no inertia, J. Fluid Mech. **879**, 793 (2019).
[38] D. T. J. Hurle, E. Jakeman, and E. R. Pike, On the solution of the Bénard problem with boundaries of finite conductivity, Proc. R. Soc. London A **296**, 469 (1967).
[39] J. M. Hewitt, D. P. McKenzie, and N. O. Weiss, Large aspect ratio cells in two-dimensional thermal convection, Earth Planet. Sci. Lett. **51**, 370 (1980).
[40] R. J. A. M. Stevens, D. Lohse, and R. Verzicco, Prandtl and Rayleigh number dependence of heat transport in high Rayleigh number thermal convection, J. Fluid Mech. **688**, 31 (2011).

[41] P. P. Vieweg, J. D. Scheel, and J. Schumacher, Supergranule aggregation for constant heat flux-driven turbulent convection, Phys. Rev. Research **3**, 013231 (2021).
[42] S.-I. Takehiro, M. Ishiwatari, K. Nakajima, and Y.-Y. Hayashi, Linear stability of thermal convection in rotating systems with fixed heat flux boundaries, Geophys. Astrophys. Fluid Dyn. **96**, 439 (2002).
[43] M. A. Calkins, K. Hale, K. Julien, D. Nieves, D. Driggs, and P. Marti, The asymptotic equivalence of fixed heat flux and fixed temperature thermal boundary conditions for rapidly rotating convection, J. Fluid Mech. **784**, R2 (2015).
[44] M. Sprague, K. Julien, E. Knobloch, and J. Werne, Numerical simulation of an asymptotically reduced system for rotationally constrained convection, J. Fluid Mech. **551**, 141 (2006).
[45] K. Julien, A. M. Rubio, I. Grooms, and E. Knobloch, Statistical and physical balances in low Rossby number Rayleigh-Bénard convection, Geophys. Astrophys. Fluid Dyn. **106**, 392 (2012).
[46] A. Sakuraba and P. H. Roberts, Generation of a strong magnetic field using uniform heat flux at the surface of the core, Nat. Geosci. **2**, 802 (2009).
[47] K. Hori, J. Wicht, and U. R. Christensen, The influence of thermo-compositional boundary conditions on convection and dynamos in a rotating spherical shell, Phys. Earth Planet. Inter. **196–197**, 32 (2012).
[48] H. Matsui, E. King, and B. Buffett, Multiscale convection in a geodynamo simulation with uniform heat flux along the outer boundary, Geochem. Geophys. Geosyst. **15**, 3212 (2014).
[49] C. Guervilly, D. W. Hughes, and C. A. Jones, Large-scale-vortex dynamos in planar rotating convection, J. Fluid Mech. **815**, 333 (2017).
[50] J.-C. Thelen and F. Cattaneo, Dynamo action driven by convection: The influence of magnetic boundary conditions, Mon. Not. R. Astron. Soc. **315**, L13 (2000).
[51] P. J. Bushby, P. J. Käpylä, Y. Masada, A. Brandenburg, B. Favier, C. Guervilly, and M. J. Käpylä, Large-scale dynamos in rapidly rotating plane layer convection, Astron. Astrophys. **612**, A97 (2018).
[52] S. Stellmach and U. Hansen, An efficient spectral method for the simulation of dynamos in Cartesian geometry and its implementation on massively parallel computers, Geochem. Geophys. Geosyst. **9** (2008).
[53] A. J. Aguirre Guzmán, M. Madonia, J. S. Cheng, R. Ostilla-Mónico, H. J. H. Clercx, and R. P. J. Kunnen, Competition between Ekman Plumes and Vortex Condensates in Rapidly Rotating Thermal Convection, Phys. Rev. Lett. **125**, 214501 (2020).
[54] D. Lemasquerier, B. Favier, and M. Le Bars, Zonal jets at the laboratory scale: Hysteresis and Rossby waves resonance, J. Fluid Mech. **910**, A18 (2021).
[55] G. R. Sarson, C. A. Jones, and K. Zhang, Dynamo action in a uniform ambient field, Phys. Earth Planet. Inter. **111**, 47 (1999).
[56] N. E. L. Haugen and A. Brandenburg, Suppression of small scale dynamo action by an imposed magnetic field, Phys. Rev. E **70**, 036408 (2004).
[57] K.-H. Glassmeier, H.-U. Auster, and U. Motschmann, A feedback dynamo generating Mercury's magnetic field, Geophys. Res. Lett. **34** (2007).
[58] N. Gómez-Pérez and J. Wicht, Behavior of planetary dynamos under the influence of external magnetic fields: Application to Mercury and Ganymede, Icarus **209**, 53 (2010).
[59] D. Heyner, J. Wicht, N. Gómez-Pérez, D. Schmitt, H.-U. Auster, and K.-H. Glassmeier, Evidence from numerical experiments for a feedback dynamo generating Mercury's magnetic field, Science **334**, 1690 (2011).
[60] T. T. Clarté, N. Schaeffer, S. Labrosse, and J. Vidal, The effects of a Robin boundary condition on thermal convection in a rotating spherical shell, J. Fluid Mech. **918**, A36 (2021).
[61] See, www.gauss-centre.eu.
[62] Jülich Supercomputing Centre, JUWELS: Modular Tier-0/1 Supercomputer at the Jülich Supercomputing Centre, J. Large-Scale Res. Facilities **5** (2019).
[63] H. Childs, E. Brugger, B Whitlock, J. Meredith, S. Ahern, D. Pugmire, K. Biagas, M. Miller, C. Harrison, G. H. Weber *et al.*, Visit: An end-user tool for visualizing and analyzing very large data, in *High Performance Visualization—Enabling Extreme-Scale Scientific Insight*, edited by E. W. Bethel, H. Childs, and C. Hansen (Routledge, New York, 2012), pp. 357–372.
[64] J. D. Hunter, Matplotlib: A 2D graphics environment, Comput. Sci. Eng. **9**, 90 (2007).